



# Volume electron microscopy reveals human retinal mitochondria that align with reflective bands in optical coherence tomography [Invited]

DEEPAYAN KAR,<sup>1</sup>  YEON JIN KIM,<sup>2</sup> ORIN PACKER,<sup>2</sup> MARK E. CLARK,<sup>1</sup> DONGFENG CAO,<sup>1</sup> CYNTHIA OWSLEY,<sup>1</sup> DENNIS M. DACEY,<sup>2</sup> AND CHRISTINE A. CURCIO<sup>1,\*</sup>

<sup>1</sup>Department of Ophthalmology and Visual Sciences, Heersink School of Medicine, University of Alabama at Birmingham, Birmingham, AL, USA

<sup>2</sup>Department of Biological Structure, University of Washington, Seattle, WA, USA

\*[christinecurcio@uabmc.edu](mailto:christinecurcio@uabmc.edu)

**Abstract:** Mitochondria are candidate reflectivity signal sources in optical coherence tomography (OCT) retinal imaging. Here, we use deep-learning-assisted volume electron microscopy of human retina and *in vivo* imaging to map mitochondria networks in the outer plexiform layer (OPL), where photoreceptors synapse with second-order interneurons. We observed alternating layers of high and low mitochondrial abundance in the anatomical OPL and adjacent inner nuclear layer (INL). Subcellular resolution OCT imaging of human eyes revealed multiple reflective bands that matched the corresponding INL and combined OPL sublayers. Data linking specific mitochondria to defined bands in OCT may help improve clinical diagnosis and the evaluation of mitochondria-targeting therapies.

© 2023 Optica Publishing Group under the terms of the [Optica Open Access Publishing Agreement](#)

## 1. Introduction

Mitochondria play key roles in energy production, calcium buffering, cell cycle and growth, signaling, aging, and regulation of innate immunity and inflammatory response, among other functions [1]. Brain mitochondria are dynamically regulated and transported along axons and dendrites to regions with high energy demands [2]. Mitochondriopathy is believed to play central roles in neurodegenerative diseases such as Alzheimer and Parkinson disease [3,4]. Direct observation of mitochondria for the purposes of screening early pathology and monitoring treatment effects, if possible, would represent progress on diseases currently with few options. As a developmental outgrowth of the brain, the retina offers such an opportunity due to the eye's transparency to light and a striking layering of cells and organelles, including mitochondria, as shown in Fig. 1. Indeed, interest in imaging the retina as a readily accessible window to brain disease, is high and increasing [5]. Further, several mitochondrial targeting drugs are in trials for age-related macular degeneration [6–8], the most common cause of irreversible vision loss in older persons worldwide.

Optical coherence tomography (OCT) is a widely used diagnostic tool for retinal disease diagnosis and management [9]. OCT detects and resolves reflections from nearly transparent cells to reveal layers of the retina and choroid. Reflections occur at boundaries between refractive indices [10]. Light scattering, i.e., redirection of light from an incident direction, occurs at refractive index gradients, for example, by water–lipid interfaces such as at the surfaces of membrane-bounded organelles [11]. Organelles larger than or equal to the wavelength of incident light (~1  $\mu\text{m}$  in diameter) can contribute to changes in OCT reflectivity, as explained by principles of Mie scattering [12–16]. For instance, in cultured cells, mitochondria and lysosomes have been shown by organelle depletion studies to strongly scatter light [14]. In human retina whole

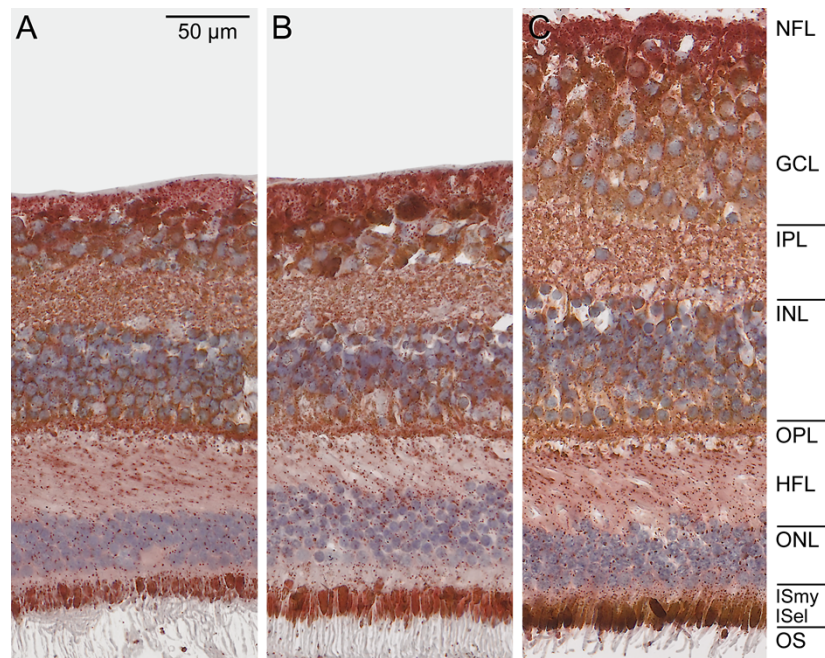


**Fig. 1.** Distribution and lamination of mitochondria in human retinal layers. Cytochrome C oxidase, subunit 4 (COX4) immunostaining of mitochondria surveyed in sections through central retina of six human donor eyes (details in Table S1 in [Supplement 1](#)). Representative parafoveal regions of (A) 94-year-old female, (B) 90-year-old, female, and (C) 83-year-old female, at 1839, 1898, and 2864  $\mu\text{m}$  eccentricities from the foveal center. COX4 immunoreactivity is strong in the ellipsoid of photoreceptor inner segments (ISel), outer (OPL) and inner (IPL) plexiform layers and ganglion cell layer (GCL). Note the strong punctate signal in the OPL, in a banded distribution. The outer nuclear (ONL) and Henle fiber (HFL) layers demonstrate relatively weak signal. NFL, nerve fiber layer; IS, photoreceptor inner segments; my, myoid; el, ellipsoid; OS, outer segments. Scale bar = 50  $\mu\text{m}$ .

mounts viewed by differential interference contrast optics, punctate reflectivities are apparent in photoreceptor inner segments, which contain numerous mitochondria [13,17,18].

An approach to determining whether human mitochondria are reflective *in vivo* is to compare mitochondrial morphology and distribution in retinal layers rich in these organelles (Fig. 1) to OCT images of the same layers. The outer plexiform layer (OPL) comprises photoreceptor axon terminals (cone pedicles and rod spherules) that contact horizontal and bipolar interneurons [19]. In mammalian retina, mitochondria are prominent in photoreceptor axon terminals of species that have a deep capillary plexus (DCP), like mouse, rat, and human. They are absent in species that lack a retinal circulation like wallaby, rabbit, and guinea pig [20]. Because mitochondria are abundant in the OPL, photoreceptor terminals and surrounding tissues can be probed for their relation to OCT reflectivity in human retina samples, without the common artifact of outer segments detaching from the retinal pigment epithelium.

Our goal, therefore, in this study is to develop the first detailed three-dimensional view of mitochondrial distributions in human OPL using volume electron microscopy, for comparison to an investigational high-resolution (HR) OCT device. The axial resolution of HR-OCT is superior to commercially available spectral domain OCT, because it uses a shorter wavelength laser and wider spectral bandwidth. By linking mitochondrial networks and OCT, we provide strong evidence that mitochondrial reflectivity can explain OPL lamination patterns and that the

OPL is a potential imaging biomarker for assessing therapies targeting these organelles. Thus, clinical OCT interpretation can be directly informed.

## 2. Design and methods

### 2.1. Tissue procurement and compliance

Retina from a 21-year male brain-dead organ donor was recovered at the termination of life support during organ recovery. Tissue was collected in collaboration with eye bank and organ procurement organizations (SightLife and Northwest LifeCenter, Bellevue, WA) and complied with regulations of the respective agencies. The study was approved by the institutional review board at the University of Washington and the University of Alabama at Birmingham. All research activities adhered to the tenets of the Declaration of Helsinki and complied with the Health Insurance Portability and Accountability Act.

### 2.2. EM sample preparation and image acquisition

The retina was maintained in vitro by dissecting retina-choroid free of the vitreous and sclera in oxygenated Ames' Medium (A1420; Sigma Chemical Co., St. Louis, MO) under light-adapted conditions for physiology experiments for a separate study. The retina was continuously superfused with Ames' medium (pH 7.3; oxygenated with 95% O<sub>2</sub>/ 5% CO<sub>2</sub>) and the temperature was thermostatically maintained within the chamber (TC-344B, Warner Instruments) at ~36 °C. Retinal tissue was rinsed thoroughly in cacodylate buffer, pH 7.4 (0.1 M), and incubated in a 1.5% potassium ferrocyanide and 2% osmium tetroxide (OsO<sub>4</sub>) solution in 0.1 M cacodylate buffer for 1 h. After washing, the tissue was placed in a freshly made thiocarbohydrazide solution (0.1 g in 10 ml double-distilled H<sub>2</sub>O heated to 60°C for 1 hour) for 20 min. After another rinse, the tissue was incubated in 2% OsO<sub>4</sub> for 30 min. The sample was rinsed again and stained en bloc in 1% uranyl acetate overnight at 40°C, washed, and stained with Walton's lead aspartate for 30 min. After a final wash, the tissue sample was dehydrated in a graded alcohol series and placed in propylene oxide for 10 min. The tissue was then embedded in epoxy resin (Durcupan, 44610, Sigma Aldrich).

The foveal center was identified using toluidine blue stained epoxy resin sections, at a point where the foveal slope levels off and the ganglion cell layer achieves minimal thickness. The imaging sample location was identified during semithin sectioning. This was approximately 800  $\mu$ m from the foveal center with a rod: cone ratio of 2.7:1 (50,257 rods and 18,516 cones per mm<sup>2</sup>) [17], illustrated in Fig. S1 in [Supplement 1](#). The tissue block was then trimmed, gold-coated by standard methods, and mounted in a Volumescope SEM (ThermoFisher). The block face was scanned at 5 nm xy resolution (incident electron beam energy, 2.2 keV, pixel dwell time of 1.5  $\mu$ s) after each of ~950, 50 nm thick sections in an array of 20, 8000  $\times$  8000 pixel (40  $\times$  40  $\mu$ m) tiles (10% tile overlap). The resulting set of ~16,000 TIFF images were contrast normalized, stitched into composite layers, then aligned into a volume using within layer and across layer procedures available with TrakEM2 software (NIH FIJI plugin).

### 2.3. Deep learning ground truth generation and volume reconstruction

Manual reconstructions of neurons and mitochondria was annotated using TrakEM2 (FIJI, National Institutes of Health, Bethesda, MD) [21,22] by an experienced grader. Mitochondria were identified by the presence of cristae inside the intermembranous matrix, and in some instances seen to span the entire diameter of the organelle lumen. Ground truth comprised of 5 vertical sections used for training and 5 vertical sections used for validation (not included in the training dataset). Complete manual annotations of mitochondria in each section were performed by an experienced grader (DK) using a pen tablet (Wacom Cintiq 22HDT). The annotated sections were approximately 7.5  $\mu$ m apart and encompassed the INL, OPL and the inner third of the Henle

fiber layer. Determination of whether an organelle was a mitochondrion was made by viewing serial sections, i.e., did 2-3 sections preceding and succeeding the reference section also contain a mitochondrion. Photoreceptors and bipolar interneurons were first skeletonized by creating nodes at the dendritic processes and then annotated using the pen tablet.

Using this manually generated ground truth, annotations were imported into Dragonfly 2020.1 (Object Research Systems, Montréal, Canada). A U-Net convolutional neural network model was trained in 68 epochs using a patch size of  $128 \times 128$  pixels taken from each image plane (yielding about 62,500 patches/image). Model inference was performed on a  $\sim 75$  GB volume comprising of 925 vertical sections (voxel size  $5 \times 5 \times 50$  nm). Dice coefficient was calculated to assess model performance. Slice-by-slice contouring was performed on the model inference to generate registered Z-stack. 3D models were exported in Standard Triangle Language (STL) format and rendered in Blender 3.0 (Blender Foundation, Amsterdam).

#### 2.4. Estimation of total number of mitochondria

To compare across histologic imaging validation studies, we estimated the number of organelles that were analyzed herein. For reference, organelles mapped in retinal pigment epithelium cells range from <5000 to 193,000 [23,24]. Automated segmentation of mitochondria in this study was suitable for calculating total volume occupancy. We estimated the total number of mitochondria analyzed in the tissue block, incorporating information about the range of individual mitochondrial volumes and overall mitochondrial volume occupancy (presented in the Results). Total mitochondria count was calculated by dividing the median volume of individual mitochondria (annotated manually) in cone pedicles and bipolar dendrites by the total mitochondrial volume in our tissue block (deep learning-enabled segmentation). Calculating a true mitochondria count requires additional information about the proportions of each cell type and class with distinctive mitochondrial morphology [25], which was beyond the scope of the current study.

#### 2.5. Cytochrome C oxidase immunohistochemistry

Retinal tissue samples were obtained from deceased human donors ( $\geq 80$  years of age, white, non-diabetic,  $\leq 6$  hours death-to-preservation) by the Advancing Sight Network (Birmingham, AL, USA) for ongoing studies on age-related macular degeneration. Protocols were approved by institutional review at University of Alabama at Birmingham (IRB-150910011) and complied with the Health Insurance Portability and Accountability Act of 1996 and the Declaration of Helsinki. Table S1 in Supplement 1 summarizes relevant donor and eye characteristics. Globes were preserved by immersion in 4% phosphate buffered paraformaldehyde after removal of the cornea. A tissue block with fovea and optic nerve head was embedded in polyethylene glycol, 12- $\mu$ m cryosection were cut using Leica CM3050 cryostat as described [26,27]. Five serial sections per eye were stained with periodic acid Schiff hematoxylin (PASH kit, Poly Scientific R&D Corp, Cat#K047) to confirm the diagnosis. Normal regions were chosen from sections with clear and organized smooth layers, without obvious lesions or deposits, and passing through the central retina, which was recognized by the presence of the Henle fiber layer [28].

Cryosections from six donor eyes with normal maculas were processed for enzymatic colorimetric staining with anti-cytochrome c oxidase subunit 1 (COX4), following described methods [27]. Briefly, after heat-induced antigen retrieval and blocking (BLOXALL, Vector labs, Cat# SP-6000), 10% horse serum and avidin/ biotin (Vector Labs, Cat# SP-2001), cryosections were incubated with primary antibodies COX4 (1: 500, Fisher, Cat#45-960-0), horse anti-mouse secondary antibody, ABC complex solution (Vector Labs, Cat# PK-7200), and AEC horseradish peroxidase substrate (Vector Labs, Cat# SK-4200) for the desired red color. Stained sections on glass slide were scanned with a UPlanSApo 20x (20x/0.75, 00/0.17/FN26.5) and 40x (40x/0.95,



00/0.11-0.23/FN26.5) objective and a robotic microscope stage (Olympus VS120, Olympus, Japan).

### 2.6. Optical coherence tomography imaging

To examine the reflective properties of the outer plexiform layer using HR-OCT imaging, human subjects were enrolled prospectively for a cross-sectional study. Participants aged 18-35 years old with no history of diagnosed eye disease or allergies to dilating drops were eligible. Demographic information (age, sex, and ethnicity) was collected. Best-corrected Snellen visual acuity was measured using Electronic Visual Acuity Tester (JAEB Center, Tampa, FL). Objective refractive error and keratometry measurements were made using the Humphrey Autorefractor/ Keratometer Model 599 (Carl Zeiss Meditec, Inc. Dublin, CA).

An investigational spectral domain OCT device (HighRes-OCT, Heidelberg Engineering, Germany) was used for retinal imaging. Relative to the widely available Spectralis device from the same manufacturer, HR-OCT uses a light source of shorter central wavelength ( $\lambda_0 = 850$  nm) and wider spectral bandwidth ( $\Delta\lambda = 140$  nm). This results in improved in-tissue axial resolution (3  $\mu\text{m}$  optical; 1.9  $\mu\text{m}$  digital sampling). Fovea-centered 30° horizontal line scans were used to qualitatively determine the visibility of OPL laminations. These were verified quantitatively using longitudinal intensity profile analysis of regions sampled and aligned using the hypo-reflective Henle fiber layer – hyperreflective OPL border as reference plane (ImageJ, National Institutes of Health, Bethesda, MD).

## 3. Results

### 3.1. Saturated segmentation of mitochondria reveals lamination of OPL mitochondria

A human donor eye specimen from a 21-year-old male was preserved at the termination of life support during organ recovery. The parafoveal region was vertically sectioned and imaged using serial block face scanning electron microscopy (SBF-SEM) at a resolution of 5 nm in the xy plane and 50 nm in the z plane. Rapid preservation provided excellent preservation of neuronal structure, including mitochondria.

To accelerate visualization of all OPL mitochondria, we embarked on a saturated reconstruction of a tissue volume with dimensions of  $85.5 \times 83.6 \times 60.0$   $\mu\text{m}$  (total block volume 428703.0  $\mu\text{m}^3$ ) using a trained 3D U-Net convolutional neural network [29,30]. The model was trained and validated to separate mitochondria from surrounding areas lacking mitochondria. This segmentation model was then applied to a ~75 GB volume of 1201 vertical EM images for inference. The model yielded exceptional performance (Dice coefficient = 0.96) (Fig. 2, Visualization 1).

To characterize the distribution of mitochondria from model predictions, the annotated EM volume was three-dimensionally aligned to the horizontal plane of retina using photoreceptor terminals as the reference plane. Projection images of annotated z-stacks revealed the laminar distribution of mitochondria in the OPL. A longitudinal mitochondrial occupancy profile representing the percent volume occupied by mitochondria at corresponding retinal depths was computed (Fig. 2(D),(E)).

A highly organized network of thousands of individual mitochondria was observed in the OPL and adjacent INL and HFL (Henle Fiber layer, including photoreceptor axons and their ensheathing glial processes) (Fig. 3). Mitochondria occupied 7.9% (33,696  $\mu\text{m}^3$ ) of the total volume of the tissue block. Mitochondria occupied 11.7% of the total measured OPL volume, and 5.2% of the INL volume. In contrast, less than 1% of the HFL volume was occupied by mitochondria. Mitochondrial volume occupancy as a function of retinal depth is shown in Fig. 5(C).

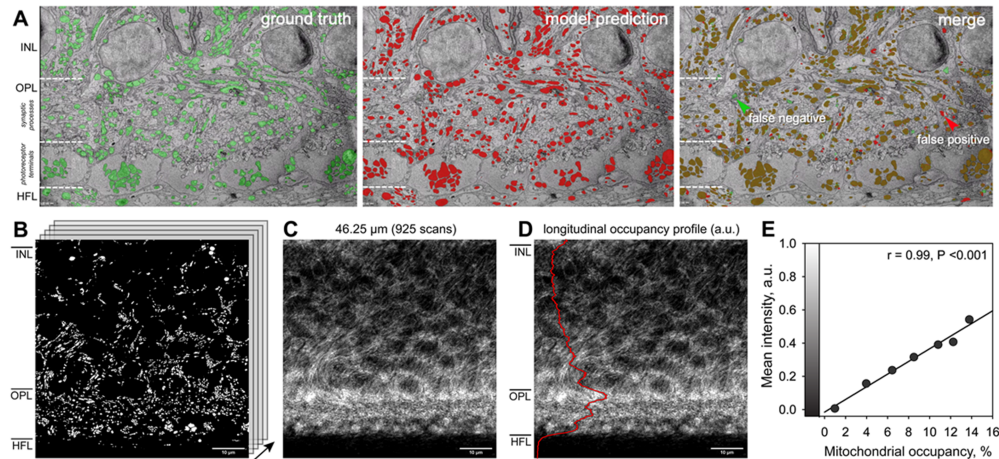


**Fig. 2.** Semantic segmentation performance and quantification of laminar distribution of mitochondria. **A.** Left: Manually annotated ground truth labelling (green) of a representative EM section used for validation of a 3D U-Net deep learning model for semantic segmentation of mitochondria. Middle: Model prediction (red) of mitochondria in the same region. Right: Merge of the ground truth and model prediction highlights correct prediction of ground truth (brown), false positive (red), and false negative (green) predictions of the model (Dice coefficient 0.96). **B.** Using mitochondria annotations predicted using deep learning-enabled model inference (white), the annotated SBF-SEM volume was three-dimensionally aligned to the horizontal axis using the mosaic of mitochondrial clusters of photoreceptor terminals as the reference plane. **C.** Projection image of annotated z-stacks reveal the laminar distribution of mitochondria in the region of interest. **D.** Longitudinal mitochondrial occupancy profile (red) represents the volume fraction of mitochondria at the corresponding retinal depth in the projection image same as Panel C. ONL, outer nuclear layer; syn, synaptic processes; cp, cone pedicles; HFL, Henle fiber layer. **E.** Scatter plot shows relationship between mean intensity (arbitrary units) of corresponding regions in projection images and mitochondrial volume occupancies (% of voxels in slabs illustrated in Fig. 3).

The median volumes of individual mitochondria in cone pedicles and bipolar dendrites were  $0.141 \mu\text{m}^3$  (IQR 0.169,  $N = 520$ ) and  $0.156 \mu\text{m}^3$  (IQR 0.157,  $N = 360$ ) respectively. Using these values to represent generic small and large organelles, respectively, the estimated number of mitochondria in the analyzed tissue volume falls between 216,000 to 238,978.

We defined 3 mitochondria-rich layers (from outer to inner: OPL1a, OPL2a, INLm) separated by 2 sublayers of lower mitochondrial occupancy (OPL1b, OPL2b) (Fig. 3(C)). Clustered mitochondria within photoreceptor axon terminals formed the outermost sublayer with high occupancy (OPL1a). A mitochondria-poor sublayer between these clusters and synaptic contacts of bipolar and horizontal interneurons accounted for the lower occupancy of OPL1b. OPL2a and OPL2b sublayers contained mitochondria within fine processes of these interneurons, being clustered in OPL2a (higher occupancy) and diffusely distributed in OPL2b (lower occupancy) (Fig. 3(D),(E)). The highest occupancy was observed in a mitochondria-rich sublayer (INLm) of the INL close to the inner border of OPL (Fig. 3(F),(G)). Mitochondrial occupancy of the sublayers INLa-c internal to INLm, containing cell bodies of horizontal, bipolar, and Müller glia, was overall lower and more diffusely distributed than the OPL (Visualization 2).

### 3.2. Reflective layers in OCT align with layers of mitochondria

To determine whether the OPL mitochondrial distribution had *in vivo* correlates of reflectivity, we performed high-resolution ( $3 \mu\text{m}$  axial) optical coherence tomography (HR-OCT) imaging of

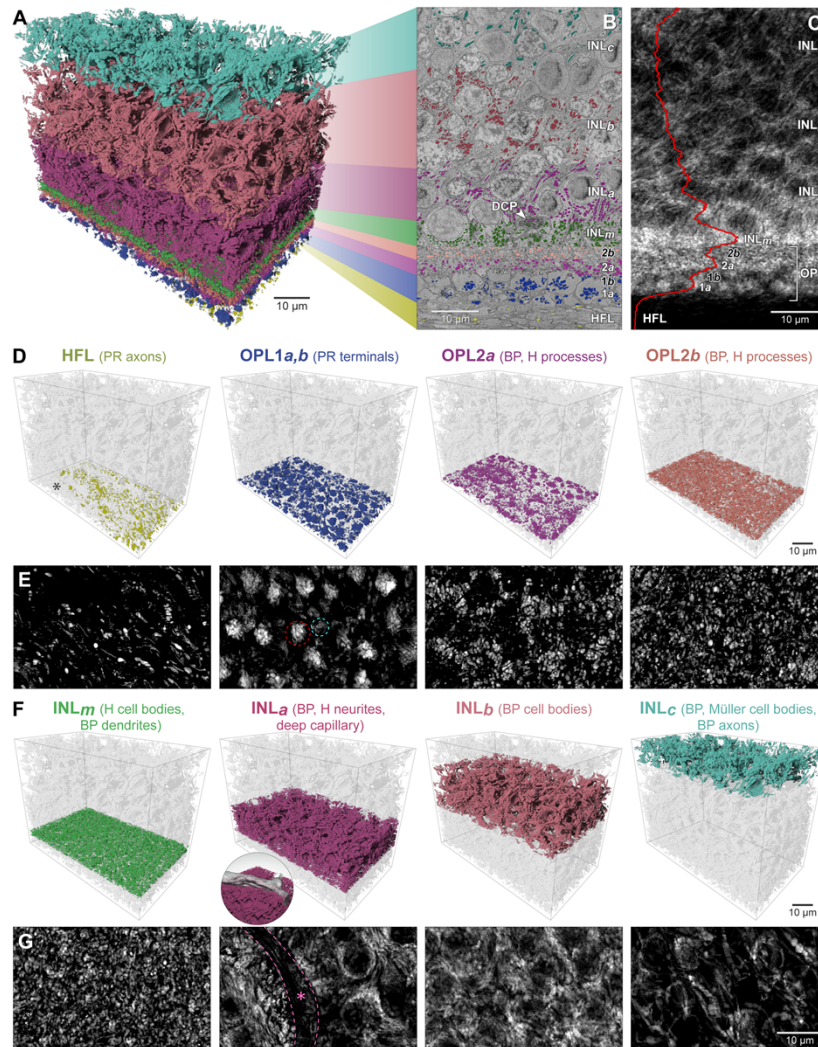


**Fig. 3.** Mitochondria form sublayers of the human retinal outer plexiform layer. A. 3D volume reconstructions of mitochondria demonstrate laminar mitochondrial distribution in the inner nuclear and outer plexiform layers of the human retina. B. Vertical section represents slabs segmented (shown in distinct colors) from the volume based on mitochondrial occupancy. C. Mitochondria occupancy in a projection image (white) and a longitudinal distribution profile (red). D, F. Volume renderings of mitochondria in the respective segmented slabs. E, G. Horizontal projection images show the mitochondrial density in the individual slabs. Red and blue dotted circles show clusters of mitochondria in a cone pedicle and a rod spherule respectively. Striking differences in mitochondrial density across the slabs demonstrate a highly organized mitochondrial distribution of the presynaptic and postsynaptic neuronal compartments.

10 human subjects. We tested the hypothesis that OPL reflectivity would precisely mirror the highly compartmentalized distribution of mitochondria shown above. Demographics and scan characteristics of the imaging study participants are detailed in Table 1.

All 10 eyes from 10 subjects (mean age 29.7 years; range 22-34 years) revealed a characteristic OPL lamination pattern, whereby two hyperreflective bands were separated by a hyporeflexive



**Table 1. Demographic and imaging characteristics of study participants (N = 10)**

| ID | Study eye | Age, years | Sex    | Ethnicity | Best-corrected visual acuity | Spherical equivalent, diopters | Scan quality (SNR), dB | OPL peak-to-peak distance, $\mu\text{m}$ |
|----|-----------|------------|--------|-----------|------------------------------|--------------------------------|------------------------|--|
| 01 | right     | 31         | female | Asian     | 20/20                        | -0.50                          | 55                     | 9.0                                      |
| 02 | right     | 29         | male   | Asian     | 20/20                        | -7.38                          | 53                     | 10.0                                     |
| 03 | left      | 24         | female | Black     | 20/20                        | +0.63                          | 52                     | 10.6                                     |
| 04 | right     | 33         | male   | White     | 20/20                        | -1.13                          | 51                     | 7.5                                      |
| 05 | left      | 31         | male   | White     | 20/15                        | 0.00                           | 49                     | 10.1                                     |
| 06 | right     | 22         | male   | White     | 20/30                        | +0.63                          | 49                     | 11.6                                     |
| 07 | right     | 29         | male   | Asian     | 20/20                        | -2.00                          | 47                     | 8.2                                      |
| 08 | right     | 34         | male   | White     | 20/20                        | -5.63                          | 47                     | 8.9                                      |
| 09 | left      | 34         | male   | Asian     | 20/20                        | -0.13                          | 46                     | 13.2                                     |
| 10 | right     | 30         | female | Black     | 20/25                        | -0.25                          | 44                     | 8.6                                      |

band (Fig. 4, Fig. 5, Fig. S2 in Supplement 1). The deep capillary plexus (DCP) appeared as regularly spaced hyperreflective spots at the inner aspect of OPL (Fig. 4). OPL laminations were prominently visible in the parafoveal and perifoveal regions of the central retina (Fig. S2 in Supplement 1). Bands were best visible in scans with high signal-to-noise ratio (Fig. 5, Fig. S2 in Supplement 1).

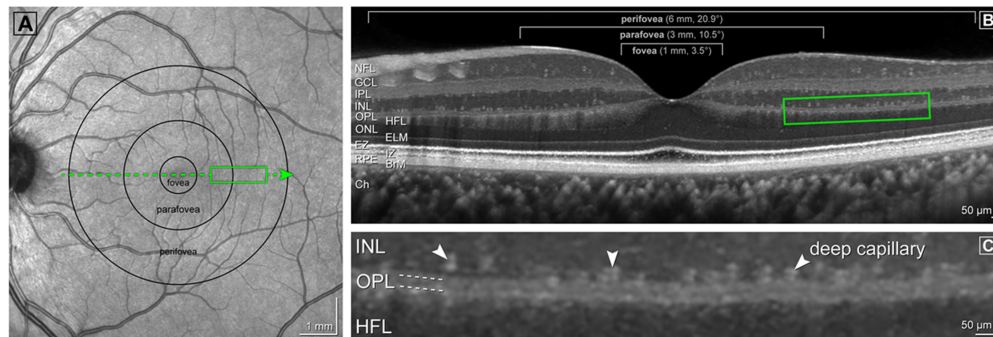


**Fig. 4.** Multimodal imaging showing representative outer plexiform layer (OPL) laminations using high-resolution optical coherence tomography (HR-OCT). A. Near infrared reflectance showing the fundus view of the retina and anatomical landmarks in a 29-year-old healthy male subject. B. Vertical cross-sectional B-scan of the macula (corresponding to green line in Panel A) passing through the foveal center in the center of the foveal pit. Visibility of retinal layers are attributed and can be distinguished by their optical reflectivity properties. C. Magnified inset of the OPL (green box in Panels A and B) demonstrate a distinct lamination pattern characterized by two hyperreflective bands (dotted lines) separated by a hyporefective band. Deep retinal capillaries are visible as distinct hyperreflective spots situated at the inner aspect of OPL (white arrowheads). The inner nuclear and Henle fiber layers appear as hyporefective bands.

The reflective properties of the OPL visible in HR-OCT appeared to align well with laminar distribution of mitochondria found using SBF-SEM (Fig. 5). To quantify the relationship to mitochondrial distribution we first assessed the separation between the outer and inner hyperreflective band (designated as band 1 and band 2 respectively), with a longitudinal profile analysis. This analysis plotted the mean normalized OCT reflectivity as a function of retinal depth (Fig. 5(B)), using the OPL boundary with the hyporefective HFL layer as a reference



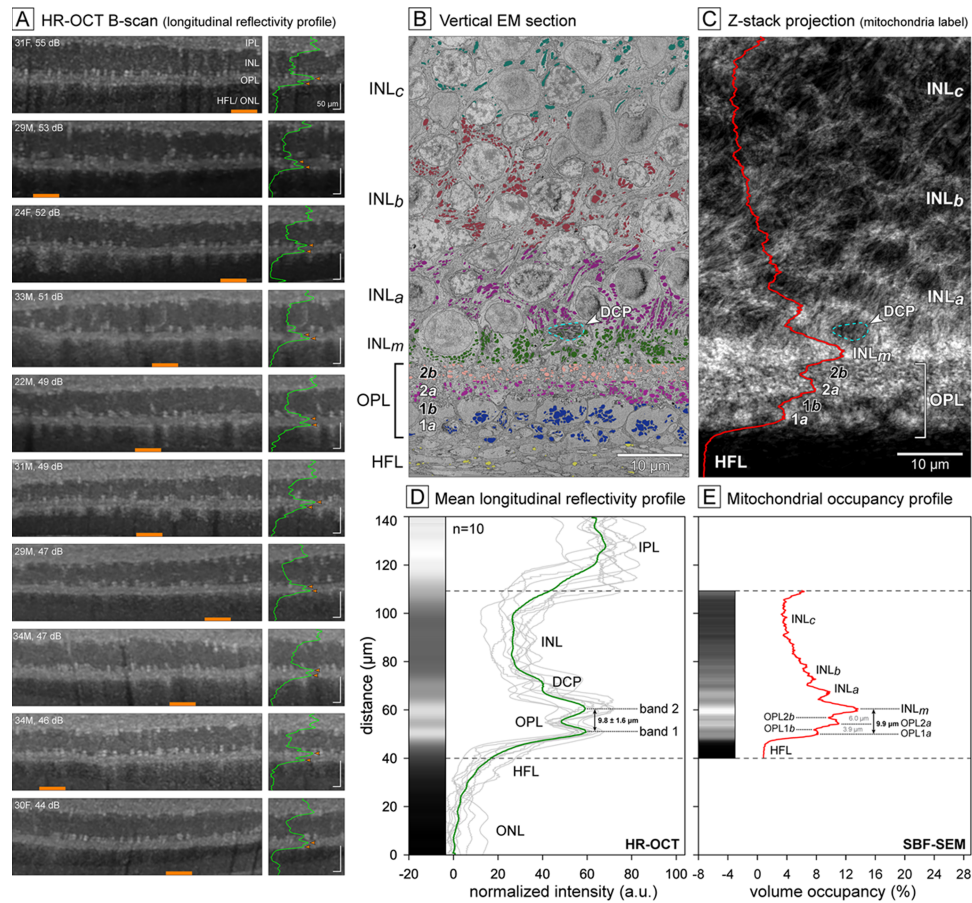


**Fig. 5.** Optical coherence tomography reveals bands correlating with ultrastructurally defined mitochondria layers. A. High resolution optical coherence tomography (HR-OCT) of the outer plexiform layer (OPL) from 10 eyes of 10 human subjects. Sampled locations from the parafoveal and perfoveal regions. Age, sex, and scan quality (signal-to-noise ratio) are indicated on the upper left of each panel. Longitudinal reflectivity profiles were generated using a standard sampling width (orange bars) and plotting the grayscale signal intensity values as a function of retinal depth (green). B. Vertical section represents slabs segmented from the volume based on mitochondrial occupancy (see Fig. 3 for details). C. Projection image and longitudinal mitochondrial distribution profile (red). Dotted line in cyan shows the location of a deep capillary plexus (DCP) vessel lumen. D. Longitudinal reflectivity curves (gray) were normalized to the signal intensity of the outer nuclear layer (which is normally hyporeflexive in healthy eyes) and aligned to the outermost hyperreflective OPL band 1. The mean longitudinal reflectivity profile is shown in green. Two hyperreflective OPL bands separated by a hyporeflexive band were identified. Peak-to-peak distances between band 1 and band 2 were quantified individually in 10 eyes. E. Mitochondrial occupancy profile shows volume fraction of mitochondria as a function of retinal depth, quantified using deep learning assisted segmentation of serial block face scanning electron microscopy data (shown in Panel C and described in Fig. 3). HR-OCT hyperreflective bands correlated with OPL sub-layers containing greater mitochondrial occupancy (~8-14%). The Henle fiber and inner nuclear layers were hyporeflexive due to lower mitochondrial occupancy (~1-4%). The peak-to-peak distances between hyperreflective outer band 1 and inner band 2 measured using HR-OCT and between INL<sub>m</sub> and OPL1a in SBF-SEM were 9.8 μm and 9.9 μm respectively. An additional OPL sub-layer of high mitochondrial occupancy (OPL2a) was not resolved by HR-OCT.

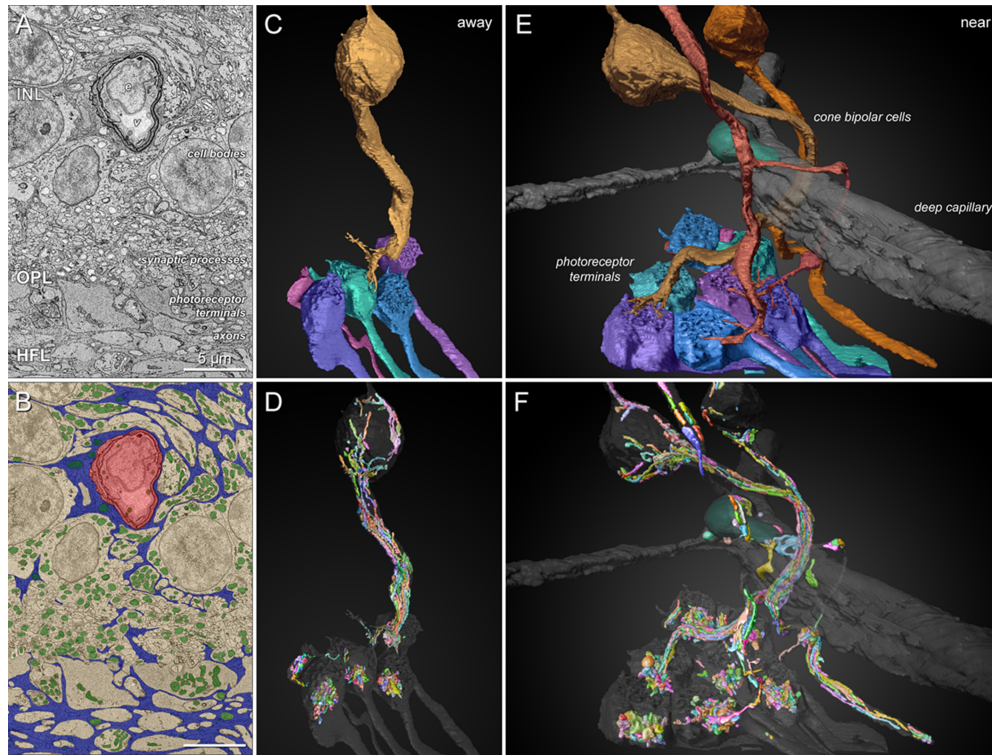


**Fig. 6.** Mitochondrial distribution in the neural-glial-vascular unit of the human photoreceptor synapse. A, B. Vertical EM section shows mitochondria (green) in neurons, glia, and vascular components of human outer plexiform layer (overlays shown in yellow, blue, and red, respectively). C. Photoreceptor axon terminals (cone pedicles and rod spherules) and a cone bipolar interneuron rendered via complete reconstructions. Note how a cone pedicle (teal) provides synaptic input to a bipolar interneuron. A rod spherule is shown in magenta. D. Ovoid mitochondria clusters occupy individual cone pedicles and morphologically different from midget bipolar interneurons containing long and slender dendritic mitochondria. Each mitochondrion is shown in a distinct color. E. Curvilinear dendritic organization of bipolar interneurons receiving input from cone pedicles adjacent to a deep capillary. F. Mitochondria arrangement in midget and diffuse bipolar interneurons conform to the curvilinear dendritic trajectory around the capillary. Like pedicles away from capillary, approximate centroids of pedicles adjacent to the capillary are occupied by ovoid mitochondria clusters. Detailed 3D renderings are shown in [Visualization 4](#).

plane. Two peaks of higher signal intensity corresponding to the hyperreflective bands were identified in all eyes (Fig. 5(A)). The mean peak-to-peak distance between outer OPL band 1 and inner OPL band 2 was  $9.8 \pm 1.6 \mu\text{m}$  (mean  $\pm$  SD, range 7.5 - 13.3  $\mu\text{m}$ ,  $n = 10$ ) when measured using HR-OCT (Fig. 5(D)). In comparison, the separation between INL<sub>m</sub> and OPL1<sub>a</sub> peak mitochondrial occupancies using SBF-SEM was 9.9  $\mu\text{m}$  (Fig. 5(E)). Despite the disparity in sample size and resolution between these two modalities, the difference between mitochondrial volume occupancy (*ex vivo*) measured using SBF-SEM and reflectivity (*in vivo*) measured using HR-OCT was only 0.1  $\mu\text{m}$ . The mitochondria-rich OPL sub-layers OPL2<sub>a</sub> and OPL1<sub>a</sub> that were visible using SBF-SEM were not resolved by HR-OCT. We identified a mitochondrial sublayer INL<sub>a</sub> located inner to the DCP (Fig. 5(C)). The maximal peak of this sublayer seemed to originate from mitochondrial densities in the bipolar dendrites that curve around the deep capillary lumen

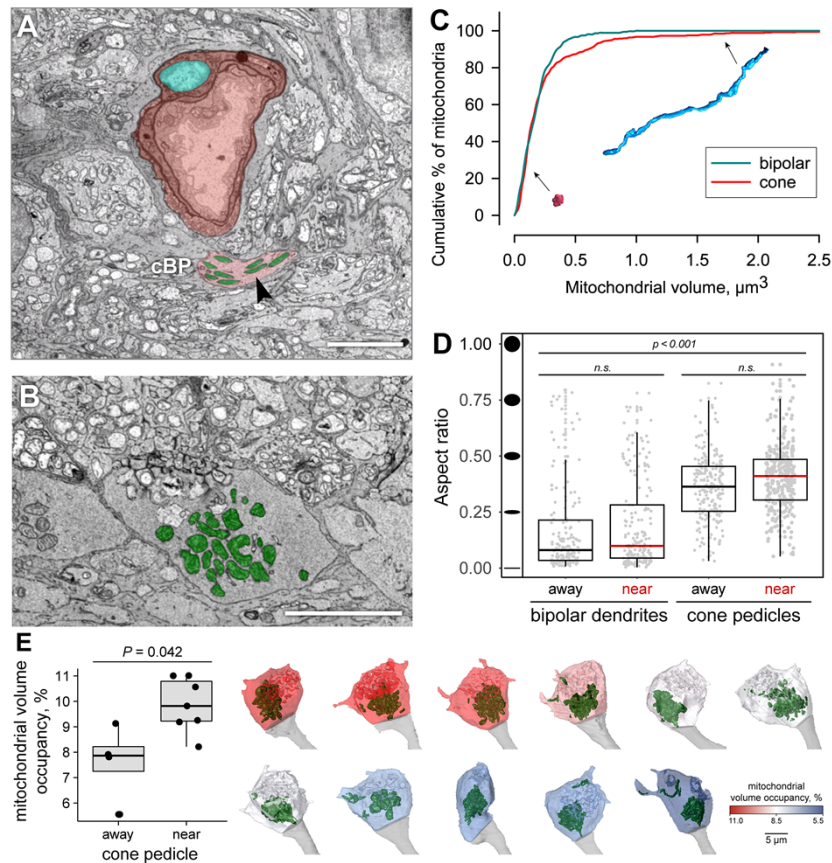


**Fig. 7.** Differences in mitochondrial morphology and shape between photoreceptors and bipolar neurons. A. EM cross-section of mitochondria (green) inside a bipolar cell dendrite encircling a deep retinal capillary. B. Ovoid mitochondrial clusters occupy the presynaptic terminals of the photoreceptor synapse. C. Cumulative frequency of distribution of mitochondria in cones and bipolar neurons. D. Boxplot showing the differences in aspect ratio of mitochondria (ratio of width to height) between mitochondria in cone pedicles and bipolar dendrites. Cone  $n = 520$  (near 292; away 228), bipolar dendrite  $n = 360$  (near 189; away 171);  $P = 0.042$ , Mann-Whitney U test. E. Cone photoreceptor terminals (pedicles) near the capillary had higher mitochondrial occupancy than cone terminals 60  $\mu\text{m}$  from capillary. Pedicles are color-coded to volume occupancy. Mitochondria clusters are shown in green. Mitochondrial volume occupancy (E), and not mitochondrial shape (defined by aspect ratio, D) differs between cone pedicles and bipolar dendrites based on the capillary eccentricity.

(Fig. 3 G, [Visualization 5](#) in Supplement). The vessels of the DCP appear as discontinuous hyperreflective dots in HR-OCT B-scans (Fig. 4).

### 3.3. Cell-type mitochondrial specializations in the anatomic OPL

To determine if most mitochondria aligned to reflective bands in OCT are in neurons, we examined mitochondrial morphology and distribution in major cell types of the OPL and DCP (Fig. 6(A),(B)). The anatomic OPL includes synapses formed by photoreceptor axons with dendrites of bipolar and horizontal cells ([Visualization 3](#)). The small rod spherules are located external to the large cone pedicles. Like ‘gems in a jewelry case’, ovoid mitochondria clustered



in the center of each cone pedicle (Fig. 6(D), (F), Fig. 7(B), [Visualization 4](#)) (mean  $54.4 \pm \text{SD } 9.7$ , range 44-66,  $n = 7$  pedicles) occupying 7-11% of each pedicle volume (Fig. 7(C)). Cone terminals near the capillary had higher mitochondrial occupancy than cone terminals located  $60 \mu\text{m}$  away from the capillary (Fig. 7(E)), near the boundary of the reconstructed block. Rod spherules had fewer mitochondria (mean  $\pm \text{SD}$ ,  $20 \pm 9$ ,  $n = 4$  rods) than cone pedicles, but were individually similar in size.

Dendrites of midganglion and diffuse bipolar interneurons curved around the capillary and contained elongated and sinuous mitochondria, conforming to the trajectory of each process (Fig. 6(F), Fig. 7(D), [Visualization 4](#), [Visualization 5](#)). Müller glial processes sheathed the entire DCP vessel. They surrounded neuronal processes but did not directly contact the capillary endothelium basement membrane (Fig. 6(B)). In serial sections, mitochondria within glia were sparse ([Visualization 5](#)). Pericytes of the DCP were recognized by a prominent nucleus and long processes covering the vascular endothelial wall (Fig. S3), containing convoluted and branching mitochondria ([Visualization 6](#)). Mitochondria in pericytes appeared similar in density across all vascular plexuses (Fig. S3). This exploration suggested that a large majority of mitochondria aligned to the OPL band of OCT are in neurons.

#### 4. Discussion

We used volume electron microscopy to show that mitochondria localize to layered sub-compartments of photoreceptors and adjacent INL cells of human retina. Using HR-OCT, we identified reflectivity bands that correspond to these sub-compartments. These data are consistent with mitochondria as major OCT signal sources, as postulated [[13,31](#)]. These findings suggest further that the current clinical consensus of a single hyperreflective OPL band can be divided into multiple sub-bands within two anatomical layers, OPL and INL [[32](#)].

We found that the peak-to-peak separation between two hyperreflective OPL bands seen with HR-OCT was almost identical ( $9.8 \mu\text{m}$  vs  $9.9 \mu\text{m}$ ) to the separation between mitochondria-rich sublayers at the INL-OPL border (INL $m$ ) and another at the level of the photoreceptor terminals (OPL1 $a$ ). The highest mitochondrial occupancy was seen in INL $m$ , located in the outer aspect of the INL close to the inner border of OPL. This is presumably the origin of the innermost band of OPL reflectivity seen on HR-OCT. OPL2 $a$  and OPL2 $b$  sublayers contain mitochondria within fine processes of horizontal and bipolar cells. While OPL2 $a$  represents a sublayer with relatively high mitochondrial occupancy, and OPL1 $a$  is separated from it by distinct sublayer of lower reflectivity, we were not able to identify corresponding separate bands in HR-OCT. This may be due to the properties of the one eye that was used for volume electron microscopy or due to the OPL1 $a$ -OPL2 $a$  distance ( $3.9 \mu\text{m}$ ) being close to the OCT resolution for this device. Studies using devices with up to  $1 \mu\text{m}$  resolution have yet to report such finely spaced bands. More samples (OCT and microscopy) may help answer this question.

While we determined that the density of mitochondria in each sublayer is related to neuron-specific occupancy, it is also characteristic to the distribution of each cell type. Externally, OPL1 $a$  and OPL1 $b$  together represent rod and cone photoreceptor terminals. OPL1 $a$  represents mitochondrial clusters in each cone pedicle or rod spherule. OPL1 $b$  represents a mitochondria-poor sublayer between these clusters and the synaptic contacts of bipolar and horizontal cells. The lower occupancy of OPL1 $b$  is due to the clustering of mitochondria in pedicles, which leaves a substantial volume of individual pedicles lacking mitochondria. The higher occupancy of the mitochondria rich sublayers OPL2 $a$  and OPL2 $b$  is due to the many dendrites of bipolar and horizontal cells. While an individual dendrite or process may have fewer individual mitochondria, the number of small-caliber processes far outnumber the photoreceptor terminals. Because mitochondria were found to occupy  $<1\%$  of the Henle fiber layer, which is normally hyporeflexive when light entry is centered in the pupil [[33](#)], we could use this layer as a reference.

Our observation of OPL lamination in human retina was preceded by suggestive evidence from others. Two reflective OPL sub-bands can be seen in adaptive optics assisted OCT images



([34] Fig. S6); the authors did not comment on this appearance. Reflective OPL sub-lamina, the inner being proportionately thicker than the outer, were illustrated in human retina using a visible light OCT prototype [35]. It was proposed that these bands may indicate cone pedicles (inner) vs rod spherules (outer) [35]. In mouse, a recent study also using visible light technology [24] illustrated a uniformly and moderately reflective band (“meso-OPL”), inner to the ONL and attributed to rod spherules in this rod-dominant species. These authors also illustrated a highly reflective and granular band (“hyper-OPL”), just internal to meso-OPL, and this was proposed as the post-synaptic processes of secondary neurons. For reference, alternating reflective bands in human retinal IPL correlated to sublayers of ON- and OFF- neural circuitry as defined by prior ultrastructural [36] and immunohistochemistry findings [37] were shown in 2010 by Tanna et al [38] and quantified in 2021 by Zhang et al [35].

Whether our OPL results support mitochondria as reflectivity sources at other retinal locations remains to be seen. For example, the effort to correlate OCT reflectivity to photoreceptor inner segment anatomy has been both intense and controversial [39–41]. Clinical consensus nomenclature for spectral domain OCT refers to the ellipsoid zone (EZ), currently being developed as an imaging biomarker for clinical trials [42]. This thick reflective band includes horizontally aligned photoreceptor inner segments, which contain numerous long, thin, mitochondria in the outer, ellipsoid portion. How mitochondria contribute to the EZ has been difficult to ascertain, for several reasons. First, the appearance of this band is device dependent. Adaptive optics-assisted OCT reveals a thin reflective band, attributed to a planar interface between the ellipsoid and outer segment, called the IS/OS junction by users of this technology [39]. Second, histologic validation of reflective bands in human eyes is challenged by artifactual bending and detachment of outer segments from supporting tissues during processing for post-mortem analysis. Third, inner segments have complex optical properties including waveguiding, refraction, and reflection that may be differentially probed by different imaging technologies [10,43]. Fourth, as shown in this report, mitochondria can differ in size and shape from one cell type to another. So far, solid evidence for mitochondria as *in vivo* signal sources at the EZ comes from several sources. Electron microscopy of pathologic human retina has shown mitochondria undergoing fission as corresponding to the reflective border of outer retinal tubulation, a glial scrolling of photoreceptors in advanced degeneration [13,44,45]. Histological measures of inner segment lengths in normal retina aligned well with the tapered outer portion of the EZ [46]. In animal models, well-designed experiments using OCT as a readout have shown strain-specific differences in reflectivity during light and dark [31] and perturbation of ellipsoid mitochondria with loss of reflectivity during hibernation [47].

Our OPL results can also help clinical interpretation of OCT images of diseases impacting the OPL. In eyes with retinal arterial occlusion, a prominent hyperreflective OPL termed as the ‘middle limiting membrane sign’ is characteristic of the acute phase of the disease [48]. Increased risk of ischemia due to higher oxygen consumption rates and altered mitochondrial density or configuration may contribute to the hyperreflectivity in the OPL/INL layers [49]. As geographic atrophy, the end-stage of AMD, develops, OPL subsidence (sinking) is a characteristic sign due to photoreceptor shortening and accompanying gliosis and is a committed step toward atrophy [50,51].

Our reconstructions show diverse and specialized mitochondrial morphologies in cells in and near the OPL. Photoreceptors terminals exhibited clusters of ovoid mitochondria centered within each terminal, whereas bipolar dendrites had long and slender mitochondria occupying the individual dendritic trajectories. Our observations in retina can be compared with those in brain assessed using volume electron microscopy [25]. Elongated mitochondria exhibit greater coupling efficiency compared to smaller punctate mitochondria, promoting effective mitochondria-dependent ATP synthesis [52–54]. A simple morphology facilitates axonal trafficking along microtubules through narrow axons [55] and specifically along photoreceptor

axon microtubules in the HFL [56,57]. Specialized morphology helps transport and positioning of organelles within the neuron to meet metabolic demands and neurovascular coupling [58]. In this context, mitochondrial distribution within the OPL may be guided by the local metabolic economy, in which the retinal microcirculation is integral. Mitochondria are prominent in photoreceptor axon terminals in species with DCP and absent in species lacking a DCP or retinal circulation altogether [20]. In contrast, layers with low oxygen gradients such as the ganglion cell layer have high mitochondrial densities in neuronal bodies [20]. This phenomenon may be developmentally guided to polarize vasculature at the inner and outer ends of photoreceptors, i.e., DCP and choriocapillaris respectively [20]. Thus, multiple sublayers of OPL mitochondria suggest functionally determined oxygen gradients, even over these small distances [59].

Strengths of this study included excellent preservation of a clinically relevant human tissue. Mitochondrial density was quantified agnostically using deep learning, enabling comprehensive and semi-automated quantification of >200,000 mitochondria, which were visualizable in both cross-sectional and *en face* planes. We used a HR-OCT device that offered better axial resolution than commercially available spectral domain OCT. Our study has limitations. The SBF-SEM study included only one specimen, reducing generalizability, although it was well matched demographically to our imaging study. While the eye tissues were rapidly recovered and fixed, there may be up to 10-16% tissue shrinkage due to EM processing [60]. Mitochondria in neurons were studied by cell class (bipolar, photoreceptor) and not by cell type (S vs L-M cone, midget vs diffuse bipolar types). Alignment of longitudinal reflectivity (SBF-SEM) and longitudinal mitochondrial occupancy (HR-OCT) profiles was empirically performed. Other potential factors impacting OCT reflectivity like membranes, synaptic vesicles, and nuclei were not assessed in the current study.

## 5. Conclusion

We conclude that our findings in volume EM and OCT synergistically suggest that mitochondrial distributions in and near human photoreceptor synapses can be accessed via clinical imaging. Visualizing known mitochondria-rich layers in human retina may have a practical utility in the near-term. Our results refine the basis of the clinical consensus OPL band and position the OPL as an additional imaging biomarker in clinical trials of agents targeting mitochondria in retinal disease.

**Funding.** National Eye Institute (EY01730, P51 OD010425, R01EY028282, R01EY029595); Research to Prevent Blindness; Dorsett Davis Discovery Fund; EyeSight Foundation of Alabama.

**Disclosures.** CAC receives research support from Genentech/ Hoffman LaRoche, Regeneron, Heidelberg Engineering and consults for Apellis, Astellas, Boehringer Ingelheim, Character Biosciences, and Osanni (all outside this project).

**Data availability.** All data needed to evaluate the conclusions are presented in the paper and/or the Supplementary Materials. Correspondence and requests for materials should be addressed to Christine A Curcio (christinecurcio@uabmc.edu) or Deepayan Kar (kar.deepayan@gmail.com).

**Supplemental document.** See [Supplement 1](#) for supporting content.

## References

1. R. Rizzuto, D. De Stefani, A. Raffaello, and C. Mammucari, "Mitochondria as sensors and regulators of calcium signalling," *Nat. Rev. Mol. Cell Biol.* **13**(9), 566–578 (2012).
2. A. Santuy, M. Turegano-Lopez, J. R. Rodriguez, L. Alonso-Nanclares, J. DeFelipe, and A. Merchan-Perez, "A quantitative study on the distribution of mitochondria in the neuropil of the juvenile rat somatosensory cortex," *Cereb Cortex* **28**(10), 3673–3684 (2018).
3. D. Trigo, J. J. Vitoria, and E. S. O. A. B. da Cruz, "Novel therapeutic strategies targeting mitochondria as a gateway in neurodegeneration," *Neural Regener. Res.* **18**(5), 991–995 (2023).
4. S. K. Maurya, S. Gupta, A. Bakshi, H. Kaur, A. Jain, S. Senapati, and M. S. Baghel, "Targeting mitochondria in the regulation of neurodegenerative diseases: A comprehensive review," *J. Neurosci. Res.* **100**(10), 1845–1861 (2022).
5. P. J. Snyder, J. Alber, C. Alt, L. J. Bain, B. E. Bouma, F. H. Bouwman, D. C. DeBuc, M. C. W. Campbell, M. C. Carrillo, E. Y. Chew, M. F. Cordeiro, M. R. Duenas, B. M. Fernandez, M. Koronyo-Hamaoui, C. La Morgia, R. O.

- Carare, S. R. Sadda, P. van Wijngaarden, and H. M. Snyder, "Retinal imaging in Alzheimer's and neurodegenerative diseases," *Alzheimers Dement* **17**(1), 103–111 (2021).
6. H. H. Szeto, "First-in-class cardioprotective compound as a therapeutic agent to restore mitochondrial bioenergetics," *Br J Pharmacol* **171**(8), 2029–2050 (2014).
  7. M. Benlahbib, S. Y. Cohen, N. Torrell, D. Colantuono, E. Crincoli, F. Amoroso, O. Semoun, C. Jung, and E. H. Souied, "Photobiomodulation therapy for large soft drusen and drusenoid pigment epithelial detachment in age-related macular degeneration: A Single-Center Prospective Pilot Study," *Retina* **43**(8), 1246–1254 (2023).
  8. S. N. Markowitz, R. G. Devenyi, M. R. Munk, C. L. Croissant, S. E. Tedford, R. Ruckert, M. G. Walker, B. E. Patino, L. Chen, M. Nido, and C. E. Tedford, "A Double-Masked, Randomized, Sham-Controlled, Single-Center Study with Photobiomodulation for the Treatment of Dry Age-Related Macular Degeneration," *Retina* **40**(8), 1471–1482 (2020).
  9. R. F. Spaide and C. A. Curcio, "Anatomical correlates to the bands seen in the outer retina by optical coherence tomography: literature review and model," *Retina* **31**(8), 1609–1619 (2011).
  10. D. T. Miller and K. Kurokawa, "Cellular-Scale Imaging of Transparent Retinal Structures and Processes Using Adaptive Optics Optical Coherence Tomography," *Annu. Rev. Vis. Sci.* **6**(1), 115–148 (2020).
  11. S. L. Jacques, "Optical properties of biological tissues: a review," *Phys. Med. Biol.* **58**(11), R37–R61 (2013).
  12. P. Chylek and J. Zhan, "Absorption and scattering of light by small particles: the interference structure," *Appl. Opt.* **29**(28), 3984 (1990).
  13. K. M. Litts, Y. Zhang, K. B. Freund, and C. A. Curcio, "Optical Coherence Tomography and Histology of Age-Related Macular Degeneration Support Mitochondria as Reflectivity Sources," *Retina* **38**(3), 445–461 (2018).
  14. J. D. Wilson and T. H. Foster, "Mie theory interpretations of light scattering from intact cells," *Opt. Lett.* **30**(18), 2442–2444 (2005).
  15. J. D. Wilson, W. J. Cottrell, and T. H. Foster, "Index-of-refraction-dependent subcellular light scattering observed with organelle-specific dyes," *J. Biomed. Opt.* **12**(1), 014010 (2007).
  16. J. D. Wilson, C. E. Bigelow, D. J. Calkins, and T. H. Foster, "Light scattering from intact cells reports oxidative-stress-induced mitochondrial swelling," *Biophys. J.* **88**(4), 2929–2938 (2005).
  17. C. A. Curcio, K. R. Sloan, R. E. Kalina, and A. E. Hendrickson, "Human photoreceptor topography," *J. Comp. Neurol.* **292**(4), 497–523 (1990).
  18. Q. V. Hoang, R. A. Linsenmeier, C. K. Chung, and C. A. Curcio, "Photoreceptor inner segments in monkey and human retina: mitochondrial density, optics, and regional variation," *Vis Neurosci* **19**(4), 395–407 (2002).
  19. S. Haverkamp, U. Grunert, and H. Wässle, "The cone pedicle, a complex synapse in the retina," *Neuron* **27**(1), 85–95 (2000).
  20. J. Stone, D. van Driel, K. Valter, S. Rees, and J. Provis, "The locations of mitochondria in mammalian photoreceptors: relation to retinal vasculature," *Brain Res.* **1189**, 58–69 (2008).
  21. A. Cardona, S. Saalfeld, J. Schindelin, I. Arganda-Carreras, S. Preibisch, M. Longair, P. Tomancak, V. Hartenstein, and R. J. Douglas, "TrakEM2 software for neural circuit reconstruction," *PLoS One* **7**(6), e38011 (2012).
  22. J. Schindelin, I. Arganda-Carreras, E. Frise, V. Kaynig, M. Longair, T. Pietzsch, S. Preibisch, C. Rueden, S. Saalfeld, B. Schmid, J. Y. Tinevez, D. J. White, V. Hartenstein, K. Eliceiri, P. Tomancak, and A. Cardona, "Fiji: an open-source platform for biological-image analysis," *Nat. Methods* **9**(7), 676–682 (2012).
  23. K. Bermond, C. Wobbe, I. S. Tarau, R. Heintzmann, J. Hillenkamp, C. A. Curcio, K. R. Sloan, and T. Ach, "Autofluorescent Granules of the Human Retinal Pigment Epithelium: Phenotypes, Intracellular Distribution, and Age-Related Topography," *Invest. Ophthalmol. Visual Sci.* **61**(5), 35 (2020).
  24. P. Chauhan, A. M. Kho, P. FitzGerald, B. Shibata, and V. J. Srinivasan, "Subcellular Comparison of Visible-Light Optical Coherence Tomography and Electron Microscopy in the Mouse Outer Retina," *Invest. Ophthalmol. Vis. Sci.* **63**(9), 10 (2022).
  25. N. L. Turner, T. Macrina, and J. A. Bae, *et al.*, "Reconstruction of neocortex: Organelles, compartments, cells, circuits, and activity," *Cell* **185**(6), 1082–1100.e24 (2022).
  26. S. D. Vogt, S. R. Barnum, C. A. Curcio, and R. W. Read, "Distribution of complement anaphylatoxin receptors and membrane-bound regulators in normal human retina," *Exp. Eye Res.* **83**(4), 834–840 (2006).
  27. D. Cao, B. Leong, J. D. Messinger, D. Kar, T. Ach, L. A. Yannuzzi, K. B. Freund, and C. A. Curcio, "Hyperreflective Foci, Optical Coherence Tomography Progression Indicators in Age-Related Macular Degeneration, Include Transdifferentiated Retinal Pigment Epithelium," *Invest. Ophthalmol. Vis. Sci.* **62**(10), 34 (2021).
  28. S. L. Polyak, *The Retina* (University of Chicago, Chicago, 1941).
  29. O. Ronneberger, P. Fischer, and T. Brox, "U-Net: Convolutional Networks for Biomedical Image Segmentation," in *Medical Image Computing and Computer-Assisted Intervention – MICCAI 2015* (Springer International Publishing, 2015), 234–241.
  30. A. Muller, D. Schmidt, C. S. Xu, S. Pang, J. V. D'Costa, S. Kretschmar, C. Munster, T. Kurth, F. Jug, M. Weigert, H. F. Hess, and M. Solimena, "3D FIB-SEM reconstruction of microtubule-organelle interaction in whole primary mouse beta cells," *J Cell Biol* **220**(2), 220 (2021).
  31. B. A. Berkowitz, R. H. Podolsky, K. L. Childers, T. Burgoyne, G. De Rossi, H. Qian, R. Roberts, R. Katz, R. Waseem, and C. Goodman, "Functional Changes Within the Rod Inner Segment Ellipsoid in Wildtype Mice: An Optical Coherence Tomography and Electron Microscopy Study," *Invest. Ophthalmol. Vis. Sci.* **63**(8), 8 (2022).
  32. G. Staurengi, S. Sadda, U. Chakravarthy, R. F. Spaide, and P. International Nomenclature for Optical Coherence Tomography, "Proposed lexicon for anatomic landmarks in normal posterior segment spectral-domain optical coherence tomography: the IN\*OCT consensus," *Ophthalmology* **121**(8), 1572–1578 (2014).

33. B. J. Lujan, A. Roorda, R. W. Knighton, and J. Carroll, "Revealing Henle's fiber layer using spectral domain optical coherence tomography," *Invest. Ophthalmol. Vis. Sci.* **52**(3), 1486–1492 (2011).
34. Z. Liu, K. Kurokawa, F. Zhang, J. J. Lee, and D. T. Miller, "Imaging and quantifying ganglion cells and other transparent neurons in the living human retina," *Proc Natl Acad Sci U S A* **114**(48), 12803–12808 (2017).
35. T. Zhang, A. M. Kho, and V. J. Srinivasan, "In vivo Morphometry of Inner Plexiform Layer (IPL) Stratification in the Human Retina With Visible Light Optical Coherence Tomography," *Front. Cell. Neurosci.* **15**, 655096 (2021).
36. M. A. Koontz and A. E. Hendrickson, "Stratified distribution of synapses in the inner plexiform layer of primate retina," *J. Comp. Neurol.* **263**(4), 581–592 (1987).
37. H. Wässle, "Parallel processing in the mammalian retina," *Nat. Rev. Neurosci.* **5**(10), 747–757 (2004).
38. H. Tanna, A. M. Dubis, N. Ayub, D. M. Tait, J. Rha, K. E. Stepien, and J. Carroll, "Retinal imaging using commercial broadband optical coherence tomography," *Br. J. Ophthalmol.* **94**(3), 372–376 (2010).
39. R. S. Jonnal, O. P. Kocaoglu, R. J. Zawadzki, S. H. Lee, J. S. Werner, and D. T. Miller, "The cellular origins of the outer retinal bands in optical coherence tomography images," *Invest. Ophthalmol. Vis. Sci.* **55**(12), 7904–7918 (2014).
40. R. F. Spaide, "Outer Retinal Bands," *Invest. Ophthalmol. Vis. Sci.* **56**(4), 2505–2506 (2015).
41. S. M. Bloom and I. P. Singal, "Revised Classification of the Optical Coherence Tomography Outer Retinal Bands Based on Central Serous Chorioretinopathy Analysis," *Retina* **41**(1), 181–188 (2021).
42. J. P. Ehlers, R. Zahid, P. K. Kaiser, J. S. Heier, D. M. Brown, X. Meng, J. Reese, T. K. Le, L. Lunasco, M. Hu, and S. K. Srivastava, "Longitudinal Assessment of Ellipsoid Zone Integrity, Subretinal Hyperreflective Material, and Subretinal Pigment Epithelium Disease in Neovascular Age-Related Macular Degeneration," *Oph Retina* **5**, 1204–1213 (2021).
43. J. M. Ball, S. Chen, and W. Li, "Mitochondria in cone photoreceptors act as microlenses to enhance photon delivery and confer directional sensitivity to light," *Sci. Adv.* **8**(9), eabn2070 (2022).
44. K. B. Schaal, K. B. Freund, K. M. Litts, Y. Zhang, J. D. Messinger, and C. A. Curcio, "OUTER RETINAL TUBULATION IN ADVANCED AGE-RELATED MACULAR DEGENERATION: Optical Coherence Tomographic Findings Correspond to Histology," *Retina* **35**(7), 1339–1350 (2015).
45. R. Dolz-Marco, K. M. Litts, A. C. S. Tan, K. B. Freund, and C. A. Curcio, "The Evolution of Outer Retinal Tubulation, a Neurodegeneration and Gliosis Prominent in Macular Diseases," *Ophthalmology* **124**(9), 1353–1367 (2017).
46. D. H. Ross, M. E. Clark, P. Godara, C. Huisinigh, G. McGwin, C. Owsley, K. M. Litts, R. F. Spaide, K. R. Sloan, and C. A. Curcio, "RefMoB, a Reflectivity Feature Model-Based Automated Method for Measuring Four Outer Retinal Hyperreflective Bands in Optical Coherence Tomography," *Invest. Ophthalmol. Vis. Sci.* **56**(8), 4166–4176 (2015).
47. B. S. Sajdak, B. A. Bell, T. R. Lewis, G. Luna, G. S. Cornwell, S. K. Fisher, D. K. Merriman, and J. Carroll, "Assessment of outer retinal remodeling in the hibernating 13-lined ground squirrel," *Invest. Ophthalmol. Vis. Sci.* **59**(6), 2538–2547 (2018).
48. Y. K. Chu, Y. T. Hong, S. H. Byeon, and O. W. Kwon, "In vivo detection of acute ischemic damages in retinal arterial occlusion with optical coherence tomography: a 'prominent middle limiting membrane sign'," *Retina* **33**(10), 2110–2117 (2013).
49. N. N. Osborne, R. J. Casson, J. P. Wood, G. Chidlow, M. Graham, and J. Melena, "Retinal ischemia: mechanisms of damage and potential therapeutic strategies," *Prog. Retinal Eye Res.* **23**(1), 91–147 (2004).
50. R. H. Guymer, P. J. Rosenfeld, and C. A. Curcio, *et al.*, "Incomplete Retinal Pigment Epithelial and Outer Retinal Atrophy in Age-Related Macular Degeneration: Classification of Atrophy Meeting Report 4," *Ophthalmology* **127**(3), 394–409 (2020).
51. Z. Wu, K. L. Goh, L. A. B. Hodgson, and R. H. Guymer, "Incomplete Retinal Pigment Epithelial and Outer Retinal Atrophy: Longitudinal Evaluation in Age-Related Macular Degeneration," *Ophthalmology* **130**(2), 205–212 (2023).
52. L. C. Gomes, G. Di Benedetto, and L. Scorrano, "During autophagy mitochondria elongate, are spared from degradation and sustain cell viability," *Nat. Cell Biol.* **13**(5), 589–598 (2011).
53. C. Harper, V. Gopalan, and J. Goh, "Exercise rescues mitochondrial coupling in aged skeletal muscle: a comparison of different modalities in preventing sarcopenia," *J. Transl. Med.* **19**(1), 71 (2021).
54. Z. H. Sheng and Q. Cai, "Mitochondrial transport in neurons: impact on synaptic homeostasis and neurodegeneration," *Nat. Rev. Neurosci.* **13**(2), 77–93 (2012).
55. Y. C. Li, X. Y. Zhai, K. Ohsato, H. Futamata, O. Shimada, and S. Atsumi, "Mitochondrial accumulation in the distal part of the initial segment of chicken spinal motoneurons," *Brain Res.* **1026**(2), 235–243 (2004).
56. P. S. Bernstein, N. A. Balashov, E. D. Tsong, and R. R. Rando, "Retinal tubulin binds macular carotenoids," *Invest. Ophthalmol. Vis. Sci.* **38**, 167–175 (1997).
57. E. Tanaka, T. Ho, and M. W. Kirschner, "The role of microtubule dynamics in growth cone motility and axonal growth," *J. Cell Biol.* **128**(1), 139–155 (1995).
58. C. C. Overly, H. I. Rieff, and P. J. Hollenbeck, "Organelle motility and metabolism in axons vs dendrites of cultured hippocampal neurons," *J. Cell Sci.* **109**(Pt5), 971–980 (1996).
59. R. Seager, L. Lee, J. M. Henley, and K. A. Wilkinson, "Mechanisms and roles of mitochondrial localisation and dynamics in neuronal function," *Neuronal Signal* **4**(2), NS20200008 (2020).
60. J. Bastacky, T. L. Hayes, and R. P. Gelinas, "Quantitation of shrinkage during preparation for scanning electron microscopy: Human lung," *Scanning* **7**(3), 134–140 (1985).